M Skiba et al.

Kinematic Background Discrimination Methods Using a Fully Digital Data Acquisition System for TOFOR

Kinematic Background Discrimination Methods Using a Fully Digital Data Acquisition System for TOFOR

Mateusz Skiba[a], Göran Ericsson[a], Anders Hjalmarsson [a], Carl Hellesen [a], Sean Conroy [a], Erik Andersson-Sundén [a], Jacob Eriksson [a] and JET Contributors[*]

EUROfusion Consortium, JET, Culham Science Centre, Abingdon, OX14 3DB, UK
[a]*Departement of Physics and Astronomy, Uppsala University, Sweden*

Abstract

A fully digital, prototype data acquisition system upgrade for the TOFOR neutron time-of-flight neutron spectrometer at the JET experimental fusion reactor in Culham, England, has been constructed. This upgrade, TOFu (Time-Of-Flight upgrade), enables digitisation of associated time and energy deposition information from the TOFOR scintillator detectors, facilitating discrimination of spectral background due to unrelated neutron events based on kinematic considerations. In this publication, a kinematic background discrimination method is presented using synthetic data and validated with experimental results. It is found that an improvement in signal-to-background ratio of 500 % in certain spectral regions is possible with the new DAQ system.

---

[*]See the Appendix of F. Romanelli et al., Proceedings of the 25th IAEA Fusion Energy Conference 2014, Saint Petersburg, Russia.

1   Introduction

Fusion neutron emission time-of-flight spectrometry can be used to measure various fusion plasma parameters such as the temperature and velocity distribution of different fuel ion species [1]. The technique has been successfully employed on both inertial confinement fusion facilities [2] and for TOKAMAK type devices [3] [4] . Since fusion neutron emission of plasmas sustained for an extended time period lack inherent time structure; a double scattering system with "start" and "stop" detector arrays is necessary to measure the neutron flight times in the latter case.

The time scales involved in measuring the flight times of fusion emission neutrons over experimentally practical distances are short (tens of nanoseconds). Therefore, a critical aspect of designing a fusion neutron emission time-of-flight spectrometer entails constructing a sufficiently fast data acquisition (DAQ) system, with a high level of time-alignment and synchronicity between its constituent channels.

TOFu (Time-Of-Flight upgrade) is a prototype, fully digital DAQ system upgrade for the TOFOR neutron [5] time-of-flight spectrometer at the JET experimental fusion facility in Culham, Oxfordshire, England. The electronics, setup and design considerations of TOFu has previously been described in depth [6]. The primary advantage of TOFu over the original TOFOR DAQ system is its ability to digitise the entire raw photo-multiplier signal with good absolute timing, enabling more precise control over event timing and correlation of neutron induced time and recoil proton energy deposition data. This in turn enables multi-parameter analysis which was previously not possible.

The present paper aims to describe a method for improving the signal-to-background ratio in TOFOR spectra, by employing the new capabilities enabled by TOFu.

2 Method and Modelling

2.1 The Kinematics of TOFOR

In order to perform the multi-parameter analysis enabled by the TOFu DAQ system upgrade, one must take into account the geometry of TOFOR. A schematic view of the spectrometer is shown in Figure 1. The geometry and its optimisation has previously been described in detail [7].

During operation, neutrons (marked n in the figure) enter the TOFOR system through a collimator below the primary organic plastic scintillator detector array S1. Some of those neutrons scatter elastically on hydrogen nuclei (protons) at some angle α. Thereafter, a fraction of the scattered neutrons that scattered in the direction of S2 interact with protons in this secondary scintillator array. The elastic neutron scattering recoil protons deposit their energy in the plastic, giving rise to scintillation photons which induce an electric pulse in photomultiplier tubes (PMT's). These pulses are digitised, generating time and pulse height information for both detector arrays. For the following discussion, the important aspects to note are the distance L between the primary and secondary array and the scattering angle α of the neutrons scattering in S1.
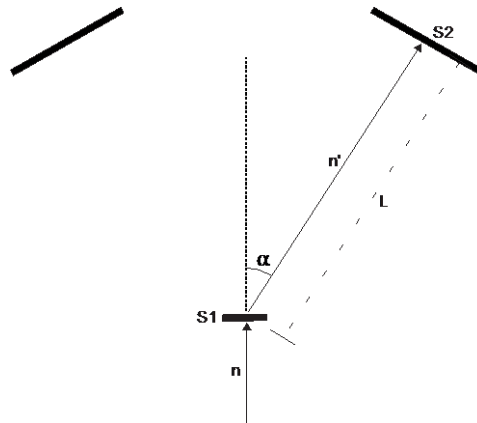
Figure 1: A schematic illustration of the TOFOR instrument. The primary and secondary scintillator arrays are denoted S1 and S2 respectively. The impinging neutrons are marked n, while the scattered neutrons are denoted by n'. The length of the flight path is known as L and the scattering angle of the scattered neutrons is α.

In the classical limit, the energy of the scattered neutrons $E_{n'}$ is given by Equation 1, where m_n is the neutron mass and v is the velocity.

$$E_{n'} = \frac{m_n v^2}{2} \tag{1}$$

The quantity measured by TOFOR is the time-of-flight t_{TOF}, related to the velocity v by the length of the flight path L as shown in Equation 2.

$$v = \frac{L(\alpha)}{t_{TOF}} \tag{2}$$

L varies with the scattering angle α, which is related to the energy of the neutron before (E_n) and after ($E_{n'}$) the elastic scattering according to Equation 3, under the approximation that the neutrons and the recoil protons are of equal mass. Note also that the exact value of L depends on the neutron interaction site within the detector arrays.

$$E_n = \frac{E_{n'}}{\cos^2 \alpha} \qquad\qquad 3$$

In elastic neutron-proton scattering events in S1, the neutron transfers a fraction of its energy to a recoil proton. The energy difference $E_n - E_{n'}$ is equal to the energy of the recoil proton E_p^{S1}, as seen in Equation 4.

$$E_p^{S1} = E_n - E_{n'} \qquad\qquad 4$$

Inserting Equations 1, 2 and 3 into 4 yields Equation 5.

$$E_p^{S1} = \frac{m_n}{2} \left(\frac{L(\alpha)}{t_{TOF}}\right)^2 \left(\frac{1}{\cos^2 \alpha} - 1\right) = \frac{m_n}{2} \left(\frac{L(\alpha)}{t_{TOF}}\right)^2 \tan^2 \alpha \qquad\qquad 5$$

As can be seen in Figure 1, the range of values that the scattering angle α can attain is limited by the spatial extension of S2, as are the values that L can have. Therefore, one can choose values of L and α in such a way that Equation 5 yields the extremum energy depositions in S1, given by Equations 6 and 7. The chosen values of L and α are defined in such a way as to represent the true, physical limits of the neutron flight path, again taking into account the spatial extension of the detector arrays, as well as the geometrical interdependence of the length of the flight path and the scattering angle.

$$E_{min}^{S1} = \frac{m_n}{2} \left(\frac{L_{min}}{t_{TOF}}\right)^2 \tan^2 \alpha_{min} \qquad\qquad 6$$

$$E_{max}^{S1} = \frac{m_n}{2} \left(\frac{L_{max}}{t_{TOF}}\right)^2 \tan^2 \alpha_{max} \qquad\qquad 7$$

These equations for the minimum and maximum recoil proton energy depositions E_{min}^{S1} and E_{max}^{S1} are vital for the continued discussion.

An upper limit may be placed on the energy deposition E_p^{S2} of recoil protons in S2 as well by noting that the scattered neutron may transfer up to its full energy upon scattering in the secondary array, and that the maximum energy available to a scattered neutron is attained by the neutrons which transfer the least amount of energy to recoil protons in S1, resulting in Equation 8.

$$E_{max}^{S2} = \frac{m_n}{2}\left(\frac{L_{min}}{t_{TOF}}\right)^2 \qquad\qquad \text{8}$$

The TOFu DAQ system enables recording of PMT pulses induced by neutrons scattering in the TOFOR S1 and S2 scintillators, simultaneously with their interaction times. As discussed previously [6], summation of the resulting, digitised waveforms provides the pulse height, which can be taken as a measure of the deposited energy of the scattering particle. In this manner, the energy depositions E_p^{S1} and E_p^{S2} of the recoil protons may be measured along with the associated t_{TOF} value, while Equations 6, 7 and 8 provide boundaries for these values.

2.2 Modelled Response of the TOFOR Instrument to a Flat Neutron Energy Distribution

The relation between t_{TOF}, E_p^{S1} and E_p^{S2} can be readily visualised with plots of 2D spectra of t_{TOF} vs. E_p^{S1} and t_{TOF} vs. E_p^{S2}. To this end, synthetic spectra displaying the response of TOFOR to a flat neutron energy distribution, ranging from 1 MeV to 18 MeV, has been produced using the Geant4 [8] [9] code. In Figure 2 a), the S1 response, with t_{TOF} on the x-axis, E_p^{S1} on the y-axis and intensity on the z-axis, is shown, along with the kinematic cuts defined by Equations 6 and 7 in red. In Figure 2 b), the corresponding S2 response is displayed. Note that in this and all similar figures henceforth, the kinematic cuts are calculated and plotted in the classical limit.

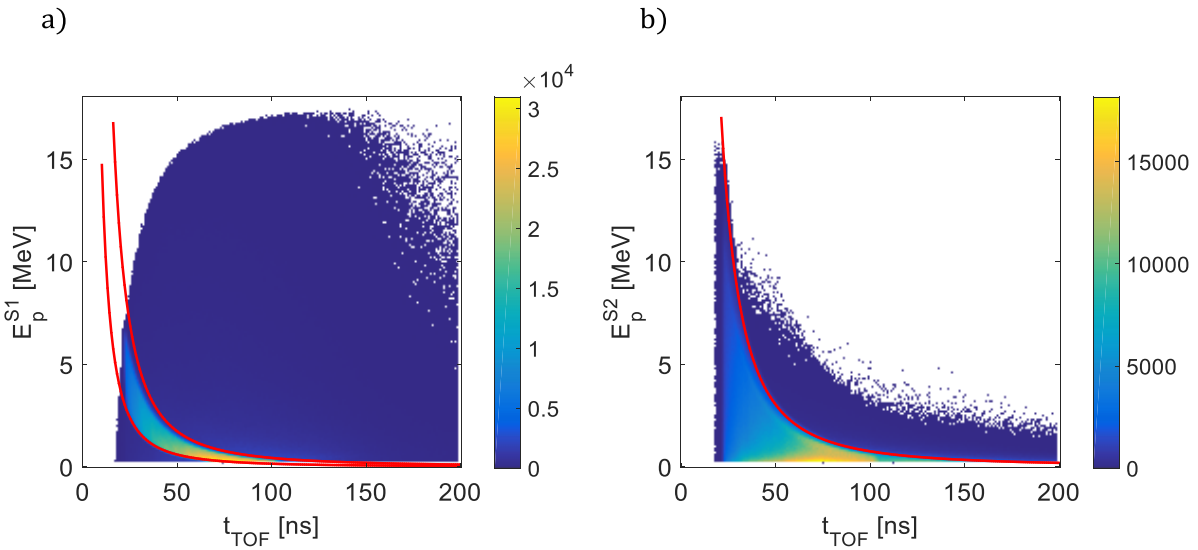Figure 2: A synthetic t_{TOF} vs. E_p spectrum for S1, with the energy cuts given by Equations 6 and 7 shown in red (a), and the corresponding S2 spectrum with the energy cut given by Equation 8 shown in red (b).

5

As evident from Figure 2, the bulk of the counts lies within the boundaries defined by Equations 6, 7 and 8. Below and beyond them, a low-intensity contribution due to multi-scattered neutrons can be seen. These events are due to all the different types of events that are not single, elastic scatterings on hydrogen nuclei, such as multi-scattering or scattering on carbon. In coincidences involving such events, the neutrons do not generally obey the relatively simple kinematic relations described in Section 2.1.

2.3 Kinematic Background Discrimination

Even though a fraction of background in TOFOR t_{TOF} spectra is comprised of events such as scattering on carbon or multiple protons in sequence, the major contribution consists of false coincidences. These occur due to S1 and S2 events caused by two separate, unrelated particles interacting within the detector arrays so close in time to each other as to be considered potentially coincident [6]. The false coincidences, or "accidentals", will form a flat background component in the t_{TOF} spectrum. Since the probability of a false coincidence occurring depends on the count rate, the relative intensity of the background component will also be rate-dependent.

Whereas the relation between t_{TOF}, and E_p^{S1} is governed by Equation 5 for true, single scattering coincidences, no such relationship exists for false coincidences. The distribution of E_p^{S1} for false coincidences is uniform in t_{TOF}, containing no time structure and depending only on the energy distribution of incident neutrons. In the same manner, the distribution of energy deposition of true coincidences in S2 is limited by Equation 8, while no such relation exists for accidentals. Therefore, if a measured energy deposition E_p^{S1} or E_p^{S2} exceeds the limits calculated by these equations for the measured, associated value of t_{TOF}, one can assume that it does not in fact partake in a true, single scattering induced coincidence. The coincidence arising from the combination of the event associated with this non-valid energy deposition and its counterpart may therefore be discarded. Note however that both events may partake separately in other, potentially valid coincidences.

2.4 The Background Component

In Figure 3, synthetic spectra of the TOFOR response to a flat neutron energy distribution ranging from 1 MeV to 18 MeV are displayed once more, this time with a finite (non-zero) neutron rate, with an S1 event rate of about 7 MHz and simulated discharge duration of nearly 1 s, resulting in the appearance of a strong false coincidence background component. Note that such a high rate, while appropriate for illustrative purposes due to the strong background component it generates, is unlikely to occur in any experimental scenarios. The t_{TOF} vs. E_p spectrum for S1 and S2 are shown in Figure 3 a) and b) respectively, with the kinematic cuts defined by Equations 6, 7 and 8 in red. In Figure 3 c), the projection of the t_{TOF} vs. E_p spectra on the t_{TOF} axis, i.e. a t_{TOF} spectrum is plotted in black. Note the relatively intense, flat background component. In addition, the negative t_{TOF} region is now shown in all three sub-plots.

By applying the kinematic cuts defined by Equations 6, 7 and 8 to the modelled data prior to constructing the spectra, as described in Section 2.3, the background events situated outside of the kinematic cuts can be removed. Projecting the remaining spectrum on the t_{TOF} axis results in the blue plot of Figure 3 c). The intensity per t_{TOF} bin of the background B is determined by Equation 9, where C_{S1} and C_{S2} are the count rates in S1 and S2 respectively and Δt is the t_{TOF} bin width.

$$B = C_{S1} C_{S2} \Delta t \qquad\qquad 9$$
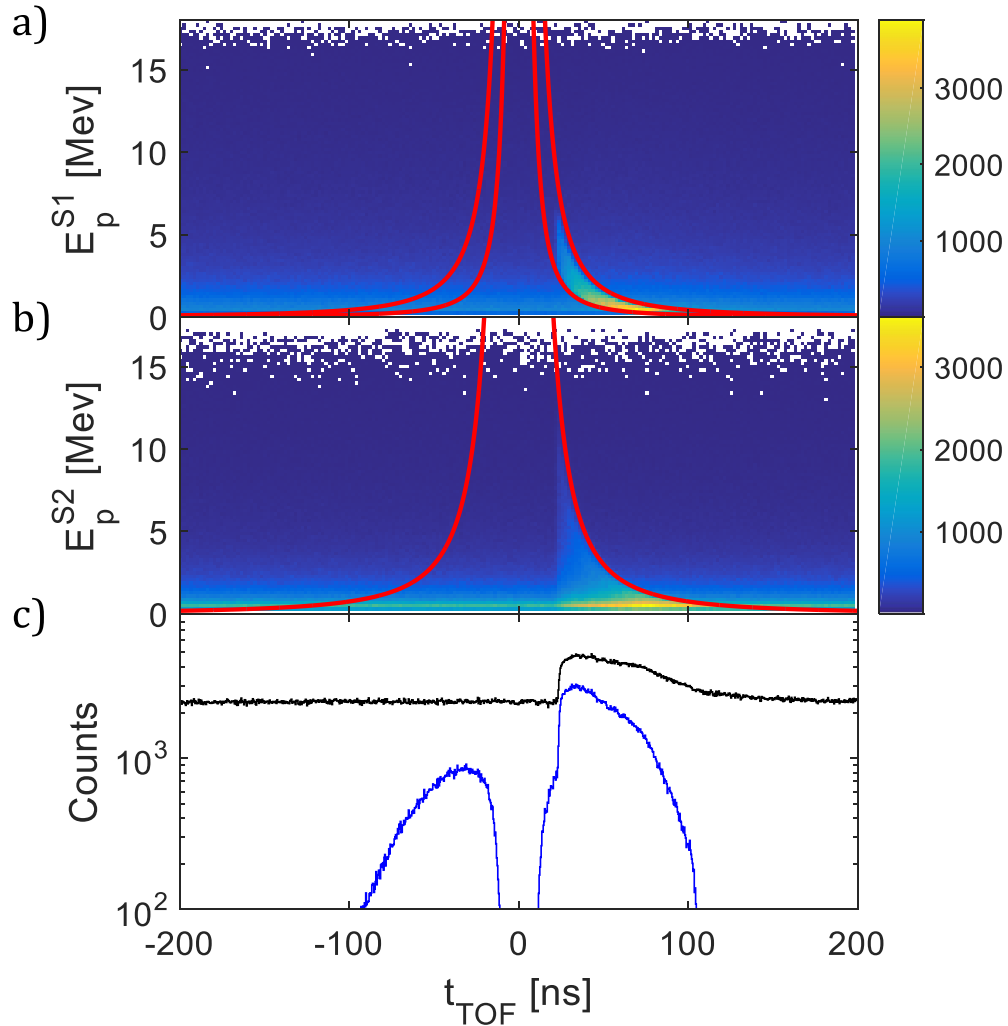
Figure 3: A synthetic t_{TOF} vs. E_p spectrum for S1, with the energy cuts given by Equations 6 and 7 shown in red (a), and the corresponding S2 spectrum with the energy cut given by Equation 8 shown in red (b). The projection on the t_{TOF} axis (i.e. the t_{TOF} spectrum) is shown in (c) black, along with the projection resulting from applying the kinematic cuts (blue), the averaged background component (red) and the projection with kinematic cuts and the averaged background component subtracted (green). The S1 event rate and discharge duration are 7 MHz and 1 s respectively.

Note that the kinematic cuts can also be applied to the negative t_{TOF} region, where no true neutron coincidences can occur, by evaluating the relevant equations for negative values of t_{TOF}. The resulting projection, as seen in the negative t_{TOF} region of Figure 3 c), shows the remaining background that cannot be removed by using the kinematic cuts.

Since the distribution of accidental background is not t_{TOF}-dependent, the shape of the background component will be similar, albeit inverted with respect to t_{TOF}, in the positive t_{TOF} region, shown in blue in Figure 3 c).

The shape of the remaining background component must be known so that it can be accounted for in analysis of t_{TOF} spectra with applied kinematic cuts. As the background component is reflected in the negative t_{TOF} region, one may simply invert with respect to t_{TOF}. The inverted background component may then be used as a fixed component in spectral analysis.

In scenarios where the neutron rate is low and the neutron statistics poor, however, the background component will be sensitive to noise. Applying the kinematic cuts to the negative t_{TOF} region will then result in a poor representation of the shape of the background component. In order to remedy this issue, one may compute a background component using averaged spectral data from the negative t_{TOF} region. This is analogous to spectra from data obtained with the original TOFOR DAQ system, where the mean of the background in the negative t_{TOF} region is used to compensate for the flat accidental coincidence component found in t_{TOF} spectra for which kinematic cuts have not been applied.

This method entails averaging the energy deposition distribution across the negative t_{TOF} range for S1 and S2, as illustrated in Figure 4 a) and d) respectively, and applying the kinematic cuts to the resulting, averaged t_{TOF} vs. E_p spectra, as seen in Figure 4 b) and e). Projecting the remaining, averaged spectra on the t_{TOF} axis, as in Figure 4 c) and f), inverting them with respect to t_{TOF} and multiplying them element-wise results in an averaged background component. The extent of the negative t_{TOF} range from which the averaged background is constructed can be made arbitrarily large in order to attain better statistics. In practice, however it must be limited in order to ensure that the plasma state and thus the neutron energy spectrum does not change significantly over the chosen time period.

In Figure 4 g), the projection of the t_{TOF} vs. E_p spectrum on the t_{TOF} axis after application of the kinematic cuts is plotted in blue; this time including both the positive and the negative t_{TOF} ranges. The averaged background component obtained with the aforementioned operations is plotted superimposed on the negative t_{TOF} range portion of the spectrum in red, but also inverted with respect to t_{TOF} in the positive region. As can be seen, the averaged background component matches the shape of the actual background resulting from applying the kinematic cuts, albeit less affected by noise. As an illustration, the spectrum after the application of the kinematic cuts with the averaged background component subtracted is shown in green in Figure 4 g) as well. Here, the background component is subtracted purely for illustration purposes; in spectral analysis it is not subtracted from the data but rather included as a fixed component.
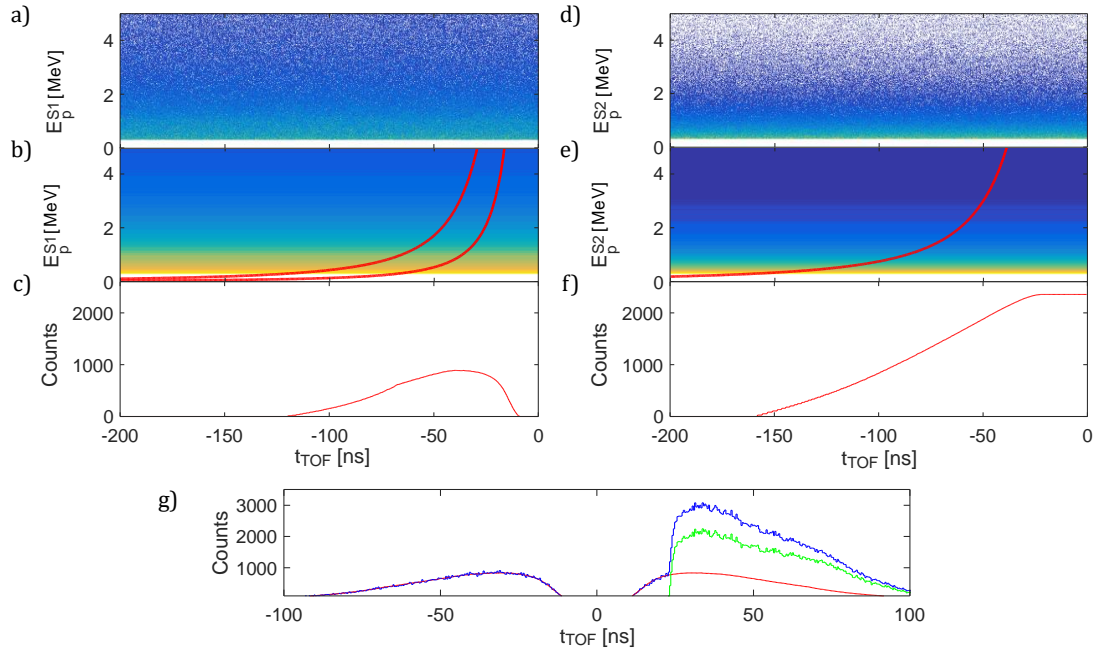
Figure 4: The procedure of constructing the averaged background component, illustrated. To the left, in a) the S1 synthetic background for the negative t_{TOF} region is shown. The averaged t_{TOF} vs E_p spectrum is displayed in b) along with the kinematic cuts and the resulting background component is shown in c). The corresponding plots for S2 are displayed in d), e) and f). The background resulting from applying the kinematic cuts to the negative t_{TOF} region is shown in g) (blue), along with the averaged background component obtained by multiplying the components from c) and f), with the result of subtracting the averaged background component from the background with kinematic cuts applied in green.

1
2 The advantage of using the averaged background component may not be apparent when viewing
3 scenarios with a relatively high event count such as the oneshown in Figure 3, since the
4 background component obtained by merely applying the kinematic cuts to the negative t_{TOF}
5 region closely resembles the averaged background component. In order to better appreciate the
6 function of the averaged background component, one may employ the averaging method on data
7 with a significantly lower event count due to a shorter discharge duration (1.5 ms), as seen in
8 Figure 5, where the background component (blue) is more severely affected by noise. As the
9 averaged background component (red) draws on a larger portion of the negative t_{TOF} region, it
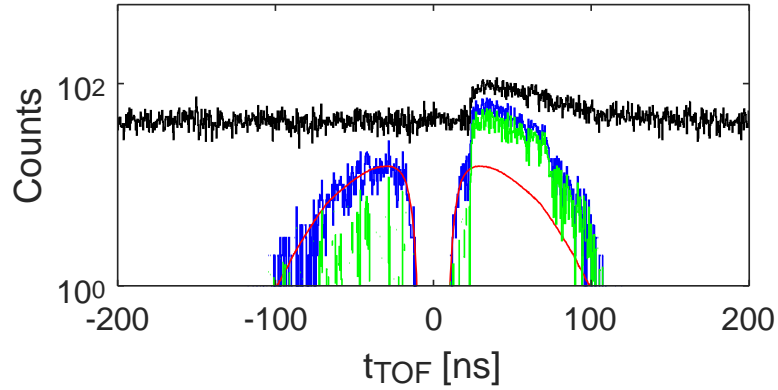10 can be more reliably employed for analysis purposes.
11

Figure 5: The projection on the t_{TOF} axis (i.e. the t_{TOF} spectrum) of a synthetic t_{TOF} vs. E_p spectrum in black with reduced statistics compared to Figure 3, along with the projection resulting from applying the kinematic cuts (blue), the averaged background component (red) and the projection with kinematic cuts and the averaged background component subtracted (green). The S1 event rate and discharge duration are 7 MHz and 1.5 ms respectively.

2.5 Energy Calibration and Resolution in Experimental Data

In experimentally obtained data, energy deposition is represented as pulse height, obtained by summation of digitised, neutron induced recoil proton scintillation pulses [6]. When applying the methods described previously in Section 2 to experimental data, it is therefore necessary to find the relationship between digitised pulse amplitude and the energy deposition E_p in S1 and S2. To this end, one may take advantage of the self-evident t_{TOF} dependence of E_p in t_{TOF} vs E_p spectra. As seen in Figure 3, there is a relatively sharp boundary between the background region and the neutron signal for a given value of t_{TOF}. In a t_{TOF} vs E_p spectrum of sufficient neutron rate, this boundary should be discernible and may be used as a reference point for mapping recorded pulse height [6] to energy deposition. However, one must take two key issues into account when performing such an energy calibration. Firstly, the recorded pulse height in experimental data is linearly dependent on the scintillator light yield, in electron-equivalent units (MeVee) rather than energy deposition in MeV. Secondly, the energy resolution of the detector assemblies (and the entire signal line) must be taken into account.

The function [10] used here for describing the relationship between light yield $l(E_p)$ in MeVee and proton energy deposition E_p in MeV, is shown in Equation 10. By identifying a known energy deposition and finding its light yield using the map in Equation 10, the conversion factor (calibration) between digitised pulse height and light yield can be estimated.

$$l(E_p) = 0.95E_p - 8.0(1 - e^{-0.1E_p^{0.9}})$$
<div align="right">10</div>

For example, one may use the electron-equivalent maximum energy transfer to recoil protons of 2.45 MeV deuterium-deuterium fusion emission neutrons. Such neutrons can generate a maximum proton recoil energy E_p = 1.0 MeV, for elastic scattering in the direction of S2. This value is obtained by inserting the extremum values of the flight path L_{max} and scattering angle α_{max} and the expected t_{TOF} = 65 ns for this neutron energy into Equation 5. The corresponding light yield energy is E_e = 0.16 MeVee. By subsequently identifying the reference pulse height value in experimental t_{TOF} vs pulse height spectra, the conversion factor between digitised data and electron-equivalent energy is estimated. In experimental data shown in the following sections, pulse height has been converted to MeV using conversion factors calculated according to this method.

The energy resolution of the TOFOR S1 and S2 detectors is not characterised. However, it may be estimated from experimental data. In general, the energy dependence of the light yield resolution of organic plastic detectors adheres to $R = K/\sqrt{E}$ [11], where K is some conversion factor such as the resolution at a reference energy. The resolution function is used to modify Equations 6, 7 and 8 while K is tuned until the kinematic cuts are sufficiently wide to allow for the majority of true coincidences to be accepted.

3 Results

In order to assess the techniques presented in the present publication, experimental data has been gathered with the TOFu DAQ system prototype and analysed according to the methods presented in Section 2. Two data sets are processed; the first being a spectrum obtained during a JET discharge heated by 3rd harmonic ICRH and the second a sum of several JET discharges between 87247 and 87371. These discharges are chosen arbitrarily, on account of being well known data sets, as the aim is to demonstrate the background discrimination method in practice rather than discuss plasma physics.

3.1 Experimental Spectrum from a 3rd Harmonic Heated Discharge

Data obtained with the TOFu DAQ prototype from the JET discharge 86775 [12] has been analysed in order to showcase the t_{TOF} dependence of the deposited energy E_p in S1 and S2. This particular discharge was heated using 3rd harmonic ICRH, which induces a fast ion population [13] resulting in a notable low-t_{TOF} (high-energy) component in t_{TOF} spectra. As can be seen in Figure 6, the resulting t_{TOF} vs. E_p spectra for S1 (a) and S2 (b) conspicuously follow the functions defined by Equations 6, 7 and 8, shown as red lines in the plots. Figure 6 may be regarded in conjunction with Figure 2 as an illustration of the adherence of the modelled spectra to the data. The highest intensity portion of the spectrum is found around 65 ns, which is the expected mean flight-time of scattered 2.45 MeV deuterium-deuterium fusion neutrons. Also visible is the contribution from γ-rays around 4 ns, which do not adhere to the kinematic principles presented in Section 2.1.

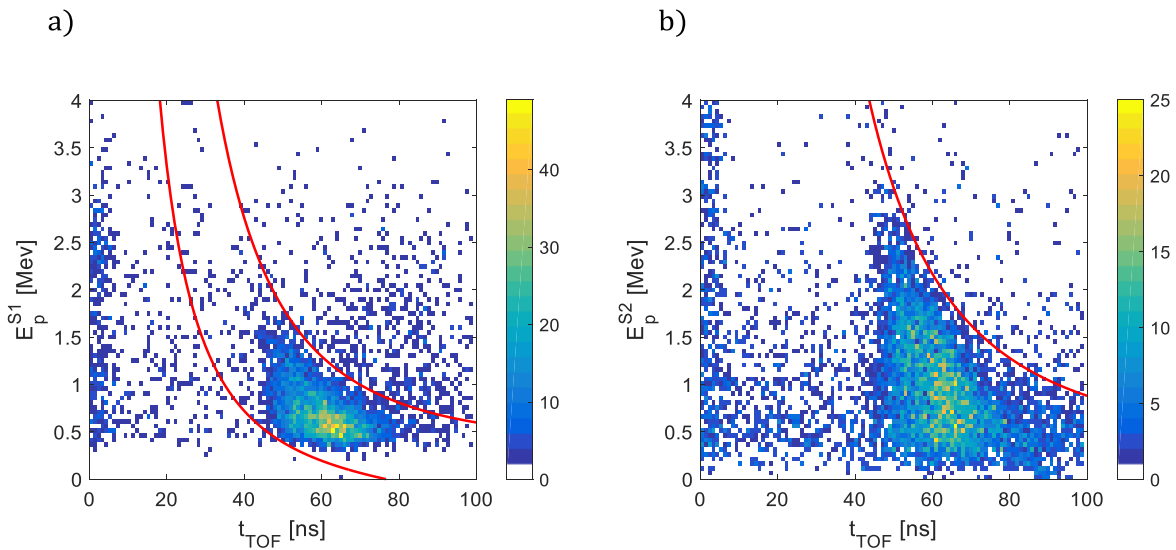a)   b)

Figure 6: A t$_{TOF}$ vs. E$_p$ spectrum for S1 obtained using TOFu of the JET discharge 86775, with the energy cuts given by Equations 6 and 7 shown in red (a), and the corresponding S2 spectrum with the energy cut given by Equation 8 shown in red (b).

3.2 Kinematic Background Discrimination in Experimental Data and Signal-to-Background Ratio

TOFu data from JET discharges ranging from 87247 to 87371 has been summed and analysed in analogy to the methods utilised on the synthetic data illustrated in Figure 3 and Figure 4, in order to demonstrate the effects of the kinematic cuts on the visibility of low-intensity spectral features. The results are shown in Figure 7, where the 65 ns, 2.45 MeV deuterium-deuterium neutron signature is clearly visible in the t_{TOF} vs. E_p spectra for S1 (a) and S2 (b). Other visible features include the γ-ray contribution around 4 ns, atmospheric μ and other γ scattering "backwards" through the TOFOR system around -5 ns and the 27 ns, 14 MeV component due to triton burnup [14] neutrons. Also shown is the t_{TOF} projection c). Note that the given energies refer to the energy of the incident neutrons, not the proton recoil energy E_p recorded by TOFu.
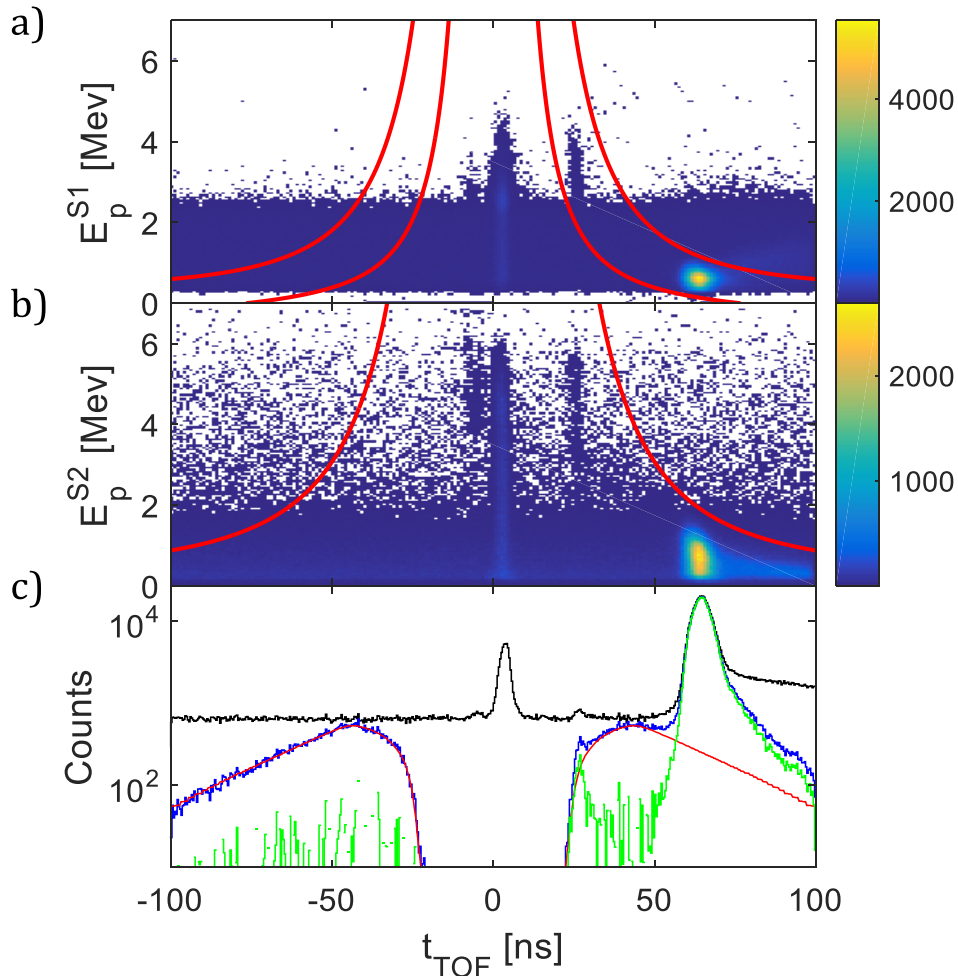

Figure 7: An experimental t_{TOF} vs. E_p spectrum from summed JET data obtained with TOFu for S1, with the energy cuts given by Equations 6 and 7 shown in red (a), and the corresponding S2 spectrum with the energy cut given by Equation 8 shown in red (b). The projection on the t_{TOF} axis (i.e. the t_{TOF} spectrum) is shown in (c) black, along with the projection resulting from applying the kinematic cuts (blue), the averaged background component (red) and the projection with kinematic cuts and the averaged background component subtracted (green).

The unprocessed projection on the t_{TOF} axis is shown in black in Figure 7 c), while the projection after application of the kinematic cuts is displayed in blue. Also shown is the averaged background component (red), calculated according to the methods described in Section 2.4 along with the difference between the projection remaining after the application of the kinematic cuts and the averaged background component (green), in analogy with Figure 4 g).

The improvement in signal-to-background ratio after application of kinematic cuts to the data has been assessed by fitting a Gaussian to the triton burnup component and comparing its integrated area in the region 22 ns – 30 ns to the integrated area of the averaged background components, computed according the methods presented in Section 2.4. After applying the kinematic cuts to the spectrum, the signal-to-background ratio of the deuterium-tritium peak improves with around 500 %, from about 1/10 to 1/2. One may note the improvement in uncertainty, as indicated by the error bars as well as the significantly improved visibility of the high energy (t_{TOF} < 25 ns) tail in the data with kinematic cuts applied.

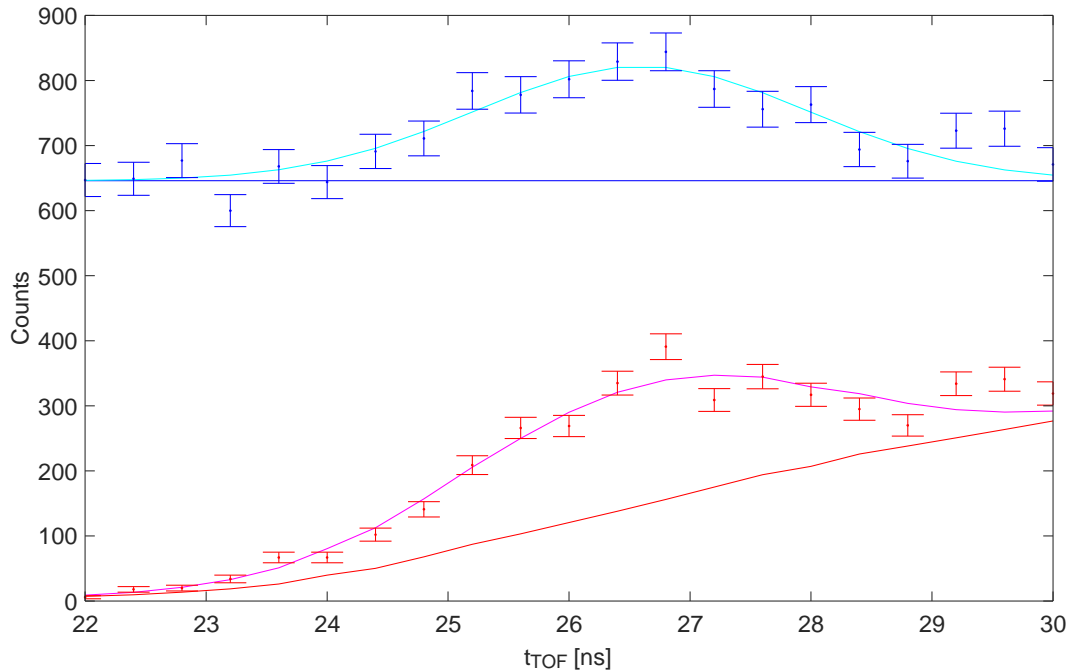**Figure 8: Time-of-flight spectrum from summed JET data obtained using TOFu, viewing the 27 ns, deuterium-tritium peak region. Spectra without (blue points) and with (red points) kinematic cuts applied are shown, along with the corresponding averaged background components (blue and red lines respectively). Gaussian fits to the deuterium-tritium signals in both scenarios are shown in cyan and magenta.**

4 Discussion and Conclusion

TOFu, the prototype DAQ system for TOFOR, has been shown to enable mitigation of spectral background comprised of false coincidences due to detector events caused by unrelated neutrons interacting within the S1 and S2 scintillator arrays. Improvements in the visibility of the deuterium-tritium fusion neutron signal in an intense random background have been demonstrated. However, the primary gains in background intensity decrease are obtained in the high-t_{TOF} (low energy) portion of t_{TOF} spectra (as seen, for example in Figure 7). This implies two situations in which the employment of the methods described in this article will provide the greatest advantage.

In deuterium-deuterium plasmas, the signal-to-background ratio of the low-energy (high-t_{TOF}) region is significantly improved which should facilitate analysis of the low energy tail of the neutron energy distribution. This will be explored in future work where the effects of kinematic background discrimination in the analysis of TOFOR spectra from deuterium-dominated plasmas will be investigated.

Secondly, one may consider scenarios with a strong high-energy (low t_{TOF}) component and a relatively weak deuterium-deuterium fusion neutron peak. A prime example of such a scenario would be a plasma with a high tritium content, where the 14 MeV neutron emission (at t_{TOF} = 27 ns) dominates the t_{TOF} spectra. In such cases, the kinematic background discrimination technique enabled by TOFu would serve to improve the visibility of the 65 ns, 2.45 MeV peak, facilitating deuterium-deuterium spectrometry that might otherwise have been difficult due to the high background contribution from false coincidences involving high-energy neutrons.

Note that while the kinematic background discrimination technique completely removes any background in the < 25 ns t_{TOF} region of TOFu spectra, that region is expected to rarely contain any signal.

It is also important to note that the geometry of TOFOR was not designed and optimised with simultaneous deuterium-tritium and deuterium-deuterium neutron spectrometry in mind. In the current configuration, the maximum possible recoil proton energy deposition of deuterium-deuterium fusion neutrons at 2.45 MeV, overlaps with the minimum energy deposition of coincident 14.0 MeV deuterium-tritium neutrons at E_p^{S1} = 1.8 MeV (Equation 6). For a future time-of-flight device for deuterium-tritium applications, one may take this into consideration in the geometric design in order to achieve separation between the deuterium-tritium and deuterium-deuterium components.

Acknowledgements

[1]   O. N. Jarvis, "Neutron measurement techniques for tokamak plasmas," *Plasma Phys. Control. Fusion*, vol. 36, no. 2, pp. 209–244, Feb. 1994.

[2]   V. Y. Glebov, T. C. Sangster, C. Stoeckl, J. P. Knauer, W. Theobald, K. L. Marshall, M. J. Shoup, T. Buczek, M. Cruz, T. Duffy, M. Romanofsky, M. Fox, A. Pruyne, M. J. Moran, R. A. Lerche, J. McNaney, J. D. Kilkenny, M. J. Eckart, D. Schneider, D. Munro, W. Stoeffl, R. Zacharias, J. J. Haslam, T. Clancy, M. Yeoman, D. Warwas, C. J. Horsfield, J.-L. Bourgade, O. Landoas, L. Disdier, G. A. Chandler, and R. J. Leeper, "The National Ignition Facility neutron time-of-flight system and its initial performance (invited)," *Rev. Sci. Instrum.*, vol. 81, no. 10, p. 10D325, 2010.

[3]   G. Grosshög, D. Aronsson, K.-H. Beimer, R. Rydz, N. G. Sjöstrand, L. O. Pekkari, and ö. Skeppstedt, "The use of the neutron-proton scattering reaction for D-T fusion spectrometry," *Nucl. Instrum. Methods Phys. Res. Sect. Accel. Spectrometers Detect. Assoc. Equip.*, vol. 249, no. 2–3, pp. 468–476, Sep. 1986.

[4]   T. Elevant, P. v. Belle, G. Grosshög, M. Hoek, O. N. Jarvis, M. Olsson, and G. Sadler, "The new JET 2.5-MeV neutron time-of-flight spectrometer," *Rev. Sci. Instrum.*, vol. 63, no. 10, p. 4586, 1992.

[5]   M. Gatu Johnson, L. Giacomelli, A. Hjalmarsson, M. Weiszflog, E. A. Sundén, S. Conroy, G. Ericsson, C. Hellesen, J. Källne, E. Ronchi, H. Sjöstrand, G. Gorini, M. Tardocchi, A. Murari, S. Popovichev, J. Sousa, R. C. Pereira, A. Combo, N. Cruz, and JET EFDA Contributors, "The TOFOR neutron spectrometer and its first use at JET," *Rev. Sci. Instrum.*, vol. 77, no. 10, p. 10E702, 2006.

[6]   M. Skiba, G. Ericsson, A. Hjalmarsson, C. Hellesen, and E. Andersson Sundén, "A Prototype Fully Digital Data Acquisition System Upgrade for the TOFOR Neutron Spectrometer at JET," *Nucl. Instrum. Methods A*, submitted for publication

[7]   M. Gatu Johnson, L. Giacomelli, A. Hjalmarsson, J. Källne, M. Weiszflog, E. Andersson Sundén, S. Conroy, G. Ericsson, C. Hellesen, E. Ronchi, H. Sjöstrand, G. Gorini, M. Tardocchi, A. Combo, N. Cruz, J. Sousa, and S. Popovichev, "The 2.5-MeV neutron time-of-flight spectrometer TOFOR for experiments at JET," *Nucl. Instrum. Methods Phys. Res. Sect. Accel. Spectrometers Detect. Assoc. Equip.*, vol. 591, no. 2, pp. 417–430, Jun. 2008.

[8]   A. Hjalmarsson, S. Conroy, G. Ericsson, L. Giacomelli, and J. Källne, "Neutron transport simulations for the design and performance optimization of the TOFOR neutron time-of-flight spectrometer," 2006.

[9]   S. Agostinelli, J. Allison, K. Amako, J. Apostolakis, H. Araujo, P. Arce, M. Asai, D. Axen, S. Banerjee, G. Barrand, F. Behner, L. Bellagamba, J. Boudreau, L. Broglia, A. Brunengo, H. Burkhardt, S. Chauvie, J. Chuma, R. Chytracek, G. Cooperman, G. Cosmo, P. Degtyarenko, A. Dell'Acqua, G. Depaola, D. Dietrich, R. Enami, A. Feliciello, C. Ferguson, H. Fesefeldt, G. Folger, F. Foppiano, A. Forti, S. Garelli, S. Giani, R. Giannitrapani, D. Gibin, J. J. Gómez

Cadenas, I. González, G. Gracia Abril, G. Greeniaus, W. Greiner, V. Grichine, A. Grossheim, S. Guatelli, P. Gumplinger, R. Hamatsu, K. Hashimoto, H. Hasui, A. Heikkinen, A. Howard, V. Ivanchenko, A. Johnson, F. W. Jones, J. Kallenbach, N. Kanaya, M. Kawabata, Y. Kawabata, M. Kawaguti, S. Kelner, P. Kent, A. Kimura, T. Kodama, R. Kokoulin, M. Kossov, H. Kurashige, E. Lamanna, T. Lampén, V. Lara, V. Lefebure, F. Lei, M. Liendl, W. Lockman, F. Longo, S. Magni, M. Maire, E. Medernach, K. Minamimoto, P. Mora de Freitas, Y. Morita, K. Murakami, M. Nagamatu, R. Nartallo, P. Nieminen, T. Nishimura, K. Ohtsubo, M. Okamura, S. O'Neale, Y. Oohata, K. Paech, J. Perl, A. Pfeiffer, M. G. Pia, F. Ranjard, A. Rybin, S. Sadilov, E. Di Salvo, G. Santin, T. Sasaki, N. Savvas, Y. Sawada, S. Scherer, S. Sei, V. Sirotenko, D. Smith, N. Starkov, H. Stoecker, J. Sulkimo, M. Takahata, S. Tanaka, E. Tcherniaev, E. Safai Tehrani, M. Tropeano, P. Truscott, H. Uno, L. Urban, P. Urban, M. Verderi, A. Walkden, W. Wander, H. Weber, J. P. Wellisch, T. Wenaus, D. C. Williams, D. Wright, T. Yamada, H. Yoshida, and D. Zschiesche, "Geant4—a simulation toolkit," *Nucl. Instrum. Methods Phys. Res. Sect. Accel. Spectrometers Detect. Assoc. Equip.*, vol. 506, no. 3, pp. 250–303, Jul. 2003.

[10] J. Frenje, "Instrumentation for fusion neutron measurements and experimentation at JET," Phd. Thesis, Acta Universitatis Upsaliensis, Uppsala universitet, 1998.

[11] G. F. Knoll, *Radiation Detection and Measurement*. John Wiley & Sons, 2010.

[12] J.-B. Girardo, S. Sharapov, J. Boom, R. Dumont, J. Eriksson, M. Fitzgerald, X. Garbet, N. Hawkes, V. Kiptily, I. Lupelli, M. Mantsinen, Y. Sarazin, M. Schneider, and JET Contributors, "Stabilization of sawteeth with third harmonic deuterium ICRF-accelerated beam in JET plasmas," *Phys. Plasmas*, vol. 23, no. 1, p. 12505, Jan. 2016.

[13] C. Hellesen, M. Gatu Johnson, E. Andersson Sundén, S. Conroy, G. Ericsson, J. Eriksson, H. Sjöstrand, M. Weiszflog, T. Johnson, G. Gorini, M. Nocente, M. Tardocchi, V. G. Kiptily, S. D. Pinches, S. E. Sharapov, and JET EFDA Contributors, "Fast-ion distributions from third harmonic ICRF heating studied with neutron emission spectroscopy," *Nucl. Fusion*, vol. 53, no. 11, p. 113009, Nov. 2013.

[14] H. Sjöstrand, G. Gorini, S. Conroy, G. Ericsson, L. Giacomelli, H. Henriksson, A. Hjalmarsson, J. Källne, D. Palma, S. Popovichev, M. Tardocchi, M. Weiszflog, and EFDA JET contributors, "Triton burn-up neutron emission in JET low current plasmas," *J. Phys. Appl. Phys.*, vol. 41, no. 11, p. 115208, Jun. 2008.